

Analysis of the physical and photoelectrochemical properties of c-Si(p)/a-SiC:H(p) photocathodes for solar water splitting

María del Carmen Mejía^{1,†}, Luis Francisco Sánchez¹, Mario Kurniawan², Lara Eggert², Alvaro Tejada^{1,3}, Magali Camargo⁴, Rolf Grieseler¹, Francisco Rumiche⁵, Isabel Díaz⁴, Andreas Bund² and Jorge Andrés Guerra^{1,‡}

¹ Departamento de Ciencias, Sección Física, Pontificia Universidad Católica del Perú, Av. Universitaria 1801, 15088, Lima, Perú.

² Technische Universität Ilmenau, Electrochemistry and Electroplating Group, Gustav-Kirch, hof-Strasse 6, 98693, Ilmenau, Germany.

³ Helmholtz-Zentrum Berlin für Materialien und Energie GmbH, Young Investigator Group for Perovskite Tandem Solar Cells, Kekuléstraße 5, 12489 Berlin, Germany.

⁴ Instituto de Corrosión y Protección, Pontificia Universidad Católica del Perú ICP-PUCP, Av. Universitaria 1801, 15088, Lima, Perú.

⁵ Departamento de Ingeniería, Sección Ingeniería Mecánica, Pontificia Universidad Católica del Perú, Av. Universitaria 1801, 15088, Lima, Perú.

E-mail: [†]maria.mejia@pucp.edu.pe, [‡]guerra.jorgea@pucp.edu.pe

August 2020

Abstract. The photoelectrochemical properties of sputtered aluminum doped hydrogenated amorphous silicon carbide thin films grown on p-type crystalline silicon substrates were investigated in 1M H₂SO₄ solution under chopped light illumination. Optical and structural properties of the top absorber layer were systematically assessed after post-deposition isochronical annealing treatments. Samples exhibited a noticeable improvement of the opto-electronic properties after thermal treatments. In addition, an abrupt enhancement of the photocurrent was observed reaching a saturation value of 17 mA/cm² at -1.75 V vs. Ag/AgCl (3.5 M KCl). In this research we propose that this enhancement effect is associated to a charge transfer kinetic mechanism influenced by surface states and the p-type substrate. The latter most likely due to the space charge region extending beyond the absorber layer reaching the substrate. Current density-potential and electrochemical impedance spectroscopy measurements in dark revealed a reduction of the SiO₂ native layer at cathodic potentials higher than -1 V vs. Ag/AgCl (3.5 M KCl), which contributes to the high charge transfer kinetic of the system. We believe that these results will contribute to understand the substrate influence in the photoelectrochemical performance of top absorber layers in multilayer structures for solar water splitting.

1. Introduction

Hydrogen is considered as a sustainable and suitable energy alternative in comparison to energy systems based on the consumption of conventional hydrocarbon fuels [1]. In particular, hydrogen production by photoelectrochemical (PEC) water splitting represents an attractive alternative to enhance the efficiency of water splitting process using sun light. Current research in this field is devoted to the fabrication and evaluation of new photoactive materials that upon sunlight absorption enable water-splitting PEC reactions with high efficiency and durability [2–6]. Most of the photoactive materials that have been investigated for solar water splitting applications exhibit poor corrosion resistance in aqueous electrolytes. On the other hand, materials for PEC water splitting are preferably made from earth-abundant and low-cost-elements using scalable devices and techniques allowing the integration of energy capture, conversion and storage in a single system [7–11].

Silicon based compounds offer a good opportunity due to the high abundance of the material and current scalable technologies. Particularly, hydrogenated amorphous silicon carbide (a-SiC:H) thin films have been tested as photocathode material for photo-assisted electrolysis, exhibiting solar to hydrogen conversion efficiencies up to 7.5 % [12]. Due to the capability to tailor the bandgap (1.8 - 3.3 eV) by the incorporation of carbon in a-Si:H, this material has turned out to be a promising candidate for PEC cells, fulfilling the optical bandgap (E_{gap}) primary requirement, i.e. $E_{\text{gap}} > 2.2 \text{ eV}$ [13,14]. Additionally, the carbon incorporation leads to an enhancement of the corrosion resistance properties in aqueous media. It has been theoretically estimated that a PEC device with an a-Si_{0.9}C_{0.1}:H absorption layer exhibiting 2.0 eV of energy bandgap, can generate a photocurrent density J_{ph} of 15 mA/cm² (solar-to-hydrogen conversion efficiency ~18 %) when submitted to an Air mass (AM) 1.5 solar spectrum [15]. Research on single thin film photoactive materials does not typically consider the role of the silicon substrate in the photoelectrochemical performance [16]. In this sense, the photoelectrode is a system formed by a p-p, n-n or n-p structure, which depending on the depth of the space charge region may have an important impact on the photoelectrode performance.

PEC performance of a-SiC:H is often limited

by its non-ideal energy band-edge alignment to the H₂O/O₂ redox potential, thus limiting the oxygen evolution reaction (OER) and the whole water splitting process [17]. To overcome this downside, an external bias needs to be applied, contributing to counteract the overpotential required to trigger the direct water splitting reaction. The external bias also contributes to reduce overpotentials due to the presence of a surface SiO₂ barrier layer and compensates interface charge carriers recombination as well.

Previous studies have demonstrated that by removing the SiO₂ native layer from a-SiC:H(i) surface, J_{ph} values over 6 mA/cm² can be achieved at a potential of -1.4 V vs. Ag/AgCl in contrast to values lower than < 4 mA/cm² obtained without the oxide removal [18]. In fact, the existence of surface states (SS) originated from the hydroxyl group termination on the oxide surface, form an electronic state that is typically located within the semiconductor bandgap [9]. The theory that such states act as recombination centers for minority photo carriers, fits quite well with the assumption that surface recombination competes with charge transfer from the semiconductor band towards the electrolyte. Additionally, it has been reported that depending on the density and energetic position of SS, these can provide another favorable pathway for indirect charge transfer to the solution, competing with the undesirable recombination mechanism [19,20]. Knowledge in this field is limited to full-drift diffusion simulations in steady-state and dynamic regimes for photo-anodic currents in crystalline materials [21,22].

Based on the steady-state and dynamic models, we have experimentally analyzed the role of surface states in the photo-cathodic current for a-SiC:H(p) top absorber layers. The effect of surface conditions and bulk opto-electronic properties of Al doped c-Si(p)/a-SiC:H(p) heterojunction photocathodes are evaluated in the present work. The photoelectrocatalytic performance is assessed before and after thermal treatments. c-Si(p) bottom absorber with a resistivity of 2.6 ohm-cm, was used as substrate for the a-SiC:H(p) layer deposition. Optical properties of the a-SiC:H(p) absorber layer were assessed systematically by means of UV-Vis transmittance measurements, from which absorption coefficient and optical bandgap were determined. Here we focus on the impact of thermal treatments on the a-SiC opto-electronic properties, the effect of the a-SiC native oxide layer, the role of localized

states, and the substrate influence on the photocurrent response of the c-Si(p)/a-SiC:H(p) photocathode system.

2. Experimental details

2.1. Photocathode fabrication

The a-SiC:H(p) thin films were deposited onto p-type $\langle 100 \rangle$ Si and fused silica substrates by reactive Radio Frequency Magnetron Co-sputtering using high purity SiC (5N) and Al (5N) targets under Ar-H₂ atmosphere mixture. Film thickness ranged around 320 nm. a-SiC:H(p) thin films on Si substrates were chosen to perform morphological, structural and photoelectrochemical characterization. Samples prepared onto fused silica substrates, were used to perform optical characterization. The Al content in the films was determined to be around 0.35 at% by Energy-dispersive X-ray spectroscopy (EDS). During the deposition processes, the substrates were cooled down with a constant flow of water at 12 °C to assure the amorphous state of the layers. Subsequently, Aluminum (20 nm) / Titanium (200 nm) contacts were deposited on the sample's corner by Radio Frequency Magnetron Sputtering applying pre-designed masks. Al was used to achieve ohmic contacts by diffusion after performing annealing treatments, while Ti was deposited on the top for mechanical stability purposes. As final step, the electrical circuit was closed using silver paste connecting the top a-SiC layer with a copper back contact.

2.2. Structural and morphological characterization

The a-SiC:H(p) layer was morphologically analyzed using Zeiss Merlin Scanning Electron Microscope with a Schottky field emission source (FESEM). X-ray diffraction patterns were recorded in the 2θ range from 15° to 70° in Grazing Incidence (GI) mode, with a glancing angle of 2°, a scan speed of 1.2 °/min and step width of 0.02°, using a Bruker D8 Discover diffractometer with Cu K α wavelength ($\lambda = 1.54 \text{ \AA}$; 40 kV, 40 mA). Finally, samples surface roughness was evaluated by Atomic Force Microscopy (AFM) before and after thermal treatments as well as before and after the exposure to 1M sulfuric acid solution. AFM measurements were carried out in an Ar-filled glovebox (M. Braun Inertgas-Systeme GmbH) using a Dimension Icon AFM device from Bruker Co.

2.3. Optical and vibrational characterization

Samples were subjected to post-deposition thermal annealing processes in a Jipelec Jetstar 100 furnace with a constant Ar flux. The annealing temperature

ranged from 200 °C to 600 °C in steps of 100 °C with an annealing time of 10 min for each heating step. More details about the heating processes can be found in [23]. The same sample was used for every heating step. After each annealing step, Current-Potential curves measurements were carried out to assess the electrical character of the contacts. Here, only as grown (AG) and 600 °C annealed samples are discussed, since only after annealing at 600 °C ohmic contacts were achieved.

Optical characterization was performed by transmittance measurements using a Perkin-Elmer UV-Vis spectrophotometer in the spectral range from 180 nm to 1500 nm. Thickness (d), refractive index (n) and absorption coefficient (α) were retrieved from transmittance spectra by a modified envelope method suitable for the determination of the fundamental absorption [24], while the optical bandgap and Urbach energy were determined using a band-fluctuations model for amorphous materials [25].

Hydrogen content and molecular bond-densities were tracked for the distinct annealing temperatures by Fourier Transform Infrared Spectroscopy (FTIR) within the range from 400 cm⁻¹ to 4000 cm⁻¹ using a Perkin-Elmer FTIR spectrometer Spectrum 1000. Owing to the baseline calibration with the Si substrate, necessary for this technique, and the fact that Si refractive index is higher than the SiC one, an additional baseline correction was performed. Details about this procedure can be found here [26].

2.4. Photoelectrochemical characterization

The photocathodes were photoelectrochemically tested using a VSP potentiostat from Bio-logic Science Instruments in a three-electrode configuration setup, where the c-Si(p)/a-SiC:H(p) heterojunction with an exposed surface area of 0.2 cm² acts as the working electrode (WE), a platinum foil as the counter electrode (CE) and a Ag/AgCl electrode (in saturated 3.5 M KCl) as a reference electrode (RE). The electrolyte was an aqueous 1M sulfuric acid (ChemSolute 95%) solution (pH = 0). Current density-voltage (J-V) curves of the photocathodes were measured at a scan rate of 5 mV/s under chopped light illumination (0.1 Hz) from simulated AM 1.5 Solar Irradiation (1000 W/m²) using a solar simulator LOT-QuantumDesign LS0108/15G.

Electrochemical impedance spectroscopy (EIS) was performed in the same solution using a potentiostat VSP-300. The frequency measurement range was 100 mHz-500 kHz with a sinusoidal potential amplitude of 15 mV. Mott-Schottky measurements were performed at fixed frequencies of 30, 40, 50 and 60 kHz. The EIS measurements were carried out for different potential values. For this purpose, the WE potential

was scanned anodically from -1.0 to 1.5 V vs. Ag/AgCl (3.5 M KCl), recording data every 35 mV. Alternating current (AC) impedance spectroscopy characterization in dark was performed by EC-LAB Analysis and Data Process software.

3. Results and discussion

3.1. Structural and morphological characterization

XRD diffractograms of the as grown and annealed sample (Fig. 1), do not show any sharp diffraction peak related to SiC crystalline phases. Therefore, after annealing at 600 °C, the SiC layer is still amorphous. The peak at $2\theta = 28^\circ$ and its shoulder at around 40° for the annealed sample, might indicate cluster formation of an amorphous carbon phase [27,28]. The presence of this phase has been corroborated by Raman measurements, as depicted in Fig. 1.

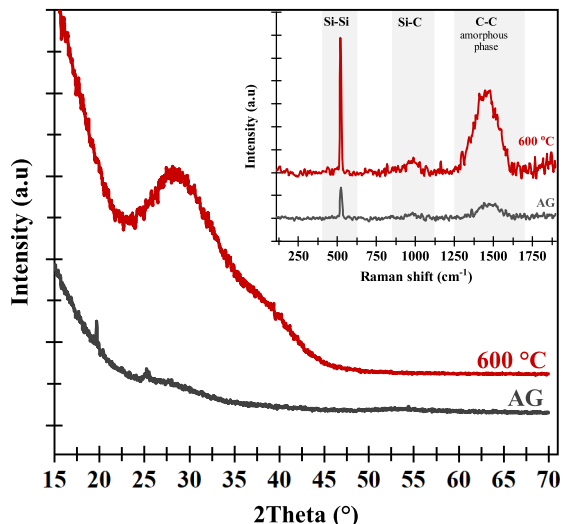


Figure 1. XRD patterns of Al doped a-SiC:H(p) in as grown (AG) state and after annealing at 600 °C. Inset depicts the Raman spectra for both cases. An increment in the Si-Si, Si-C and C-C modes is detected after the heating process

Fig. 2 depicts SEM images of the Al doped a-SiC:H(p) layers in the as grown (a) and annealed (b) states. Since both samples were deposited on the same c-Si(p) substrate and in the same location and sputtering conditions, the observed shrinking in the annealed sample is attributed to the post-deposition heat treatment. The shrinking value could be obtained by UV-Vis measurements, as will be discussed in the following section.

AFM images are shown in Fig. 3. There is no observed change in surface roughness for the sample after being photoelectrochemically tested. However, after annealing a roughness reduction from 1.04 to 0.35 nm in root-mean-square roughness R_q is observed.

3.2. Optical and vibrational characterization

Fig. 4 shows the transmittance spectra and the Tauc-plot of the absorption coefficient of a-SiC:H(p), before and after annealing at 600 °C. The fundamental absorption was fitted with the Tauc model and the band-fluctuation model defined in Eq. 1, which takes into account the overlap of the Urbach tail on the absorption edge [25]. Here, α_0 , E_{BF} and E_U are the scale factor related to the transition matrix element, the optical bandgap and the Urbach energy, respectively. $\hbar\omega$ is the photon energy and $\text{Li}_2(z)$ is the dilogarithm function of z . Retrieved parameters, before and after annealing, are summarized in Table 1.

$$\alpha(\hbar\omega) = -\frac{\pi}{4} \frac{\alpha_0 E_U^2}{\hbar\omega} \text{Li}_2 \left(-e^{E_U^{-1}(\hbar\omega - E_{BF})} \right). \quad (1)$$

Table 1. Best fit parameters for the a-SiC:H(p) absorption coefficient spectra using Eq. 1. Tauc bandgap (E_{Tauc}) and thickness (d) are given for comparison purposes.

	AG	600 °C
E_{Tauc} (eV)	2.33 ± 0.01	2.48 ± 0.01
E_{BF} (eV)	2.55 ± 0.01	2.76 ± 0.01
E_U (meV)	780 ± 10	840 ± 30
α_0 (cm ⁻¹)	$7.35\text{E}+0.5$	$7.36\text{E}+0.5$
d (nm)	321 ± 0.90	266 ± 0.51

The Urbach energy E_U is associated to disorder-induced localized states. An increase in E_U is observed after thermal treatments, i.e. from 780 meV for the as grown sample to 840 meV after annealing at 600 °C. This increase has been typically attributed to the depletion of hydrogen-related bonds [29]. However, this effect has also been observed in samples with no hydrogen content [25, 26]. This suggests that structural features related to the mean-bond length and amorphous carbon clusters formation with annealing, could be responsible for the enhancement of the Urbach tail.

A slight increment of the optical bandgap energy was also observed upon the annealing at 600 °C, from 2.55 eV to 2.76 eV. Despite the increase of E_{gap} and the reduction in the a-SiC:H(p) thin film absorption, ohmic contacts were achieved after annealing at this temperature. On the other hand, after the heating processes of the a-SiC layer, a thickness shrinking was observed from ~ 320 to ~ 265 nm. As a result, densification occurs from 3.04 to 3.12 g/cm³. Details about the thickness shrinking mechanism can be found in [23]. Density values were calculated using the refractive index taken at 800 nm wavelength, following the Lorentz-Lorentz (L-L) relation depicted in Eq. 2. Where n is the refractive index, ρ is the mass density,

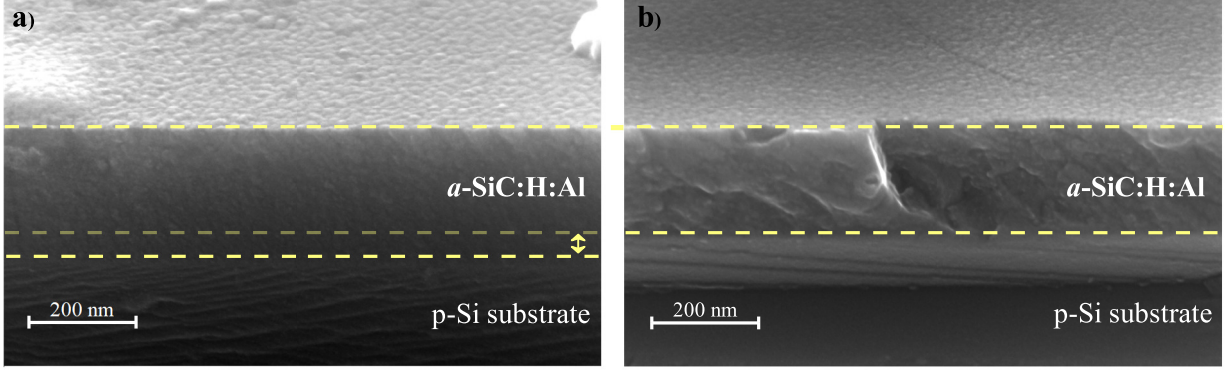


Figure 2. FESEM Tilt-section images of c-Si(p)/a-SiC:H(p) as grown sample (a) and annealed sample (b). Thickness shrinking by about 17% is highlighted. Differences in surface roughness are observed and subsequently estimated in R_q values by AFM [23].

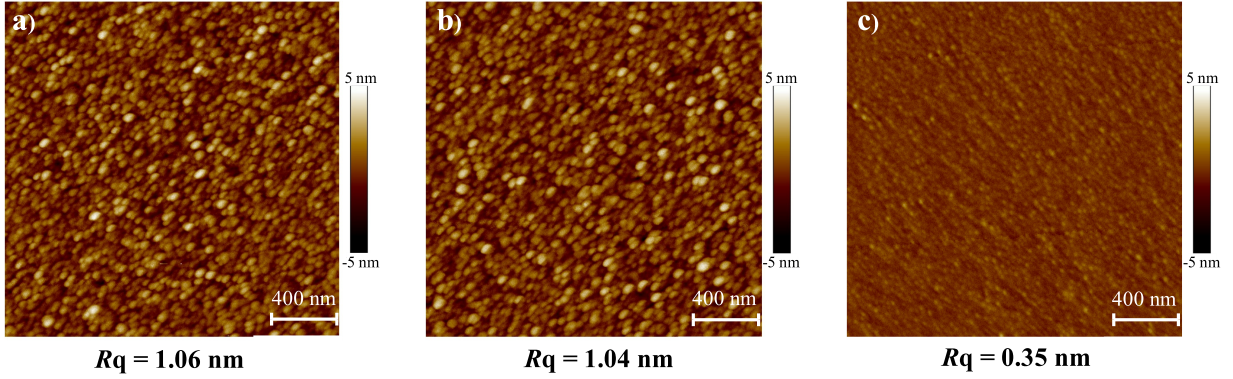


Figure 3. AFM images taken from c-Si(p)/a-SiC:H(p) sample in as grown state before being photoelectrochemically tested (a), in as grown state after photoelectrochemical test (b) and after annealing treatment at 600 °C and photoelectrochemical test (c). Root-mean-squared roughness values R_q are shown below each image.

A_0 is the Avogadro's number, M is the molecular weight and α' is the molecular electronic polarizability, which is around 1.4 \AA^3 [30].

$$\frac{n^2 - 1}{n^2 + 2} = \left(\frac{\rho A_0}{M} \right) \frac{4\pi\alpha'}{3}. \quad (2)$$

IR absorption spectra are shown in Fig. 5. Vibrational states and inverse absorption cross section values (κ) for the different bonds identified are shown in Table 2. κ values were used to calculate the bond densities (N), shown in Table 3, according to Eq. 3, where ν is the wavenumber. Si-O bonds were not identified in the bulk spectrum, however, this does not exclude the existence of the native SiO_2 layer at the semiconductor surface. It has been widely reported that SiO_2 grows spontaneously on clean SiC surfaces when it is exposed to air or solutions, exhibiting a thickness between 2-5 nm [31–33].

$$N = \kappa \int \left(\frac{\alpha(\nu)}{\nu} \right) \delta\nu. \quad (3)$$

Table 2. Vibrational states and inverse absorption cross sections (κ) for the different bonds presented in a-SiC:H thin films.

Vibrational mode	Wavenumber (cm^{-1})	Inverse abs. cross section (cm^{-2})
Si-C Asym. stretching	~ 790	2.13×10^{19}
Si- CH_n Wagging/rocking	~ 1000	2.13×10^{19}
Si-H Stretching	~ 2100	1.40×10^{20}
C-H Stretching	~ 2890	1.35×10^{21}

FTIR analysis revealed the effect of thermally-induced hydrogen out-diffusion. After annealing at 600 °C, the Si-H and C-H bonds are depleted, promoting the Si-C bond density (see Table 3).

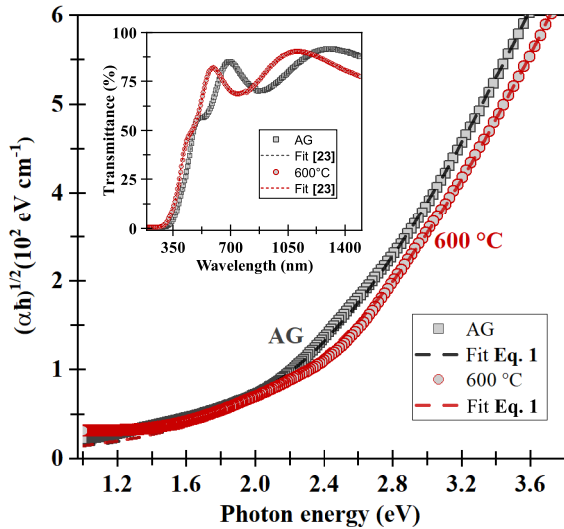


Figure 4. Transmittance spectra, absorption coefficient and corresponding fits of as grown (AG) and annealed a-SiC:H(p).

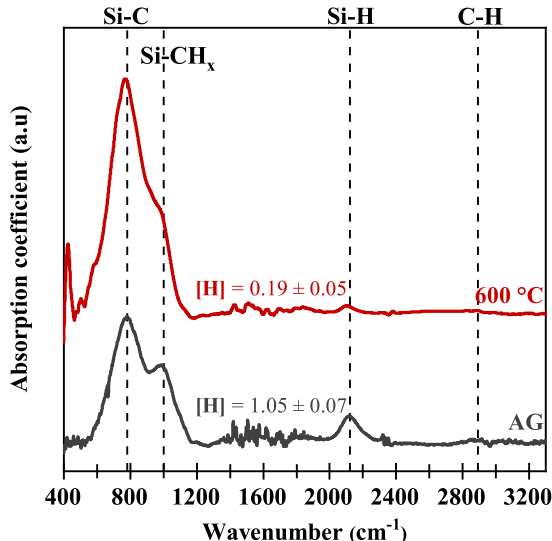


Figure 5. FTIR spectra of a-SiC:H(p) as grown (AG) and after annealing at 600 °C. Calculated values of hydrogen concentration are shown for each spectrum in 10^{21} atoms/cm³. The signals associated to the different bonding vibration modes are also highlighted.

Table 3. Bond density values ($\times 10^{21}$ atoms/cm³) for the a-SiC:H films, as grown AG and after annealing at 600 °C.

	Si-C	Si-CH _n	Si-H	C-H
AG	3.00	50.0	0.80	0.70
600 °C	50.7	80.3	0.13	0.06

3.3. Photoelectrochemical characterization

All potential values in this section are indicated relative to the Ag/AgCl (3.5 M KCl) scale. Fig. 6 depicts the recorded J_{ph} for the as grown sample and for the sample after annealing. For the as grown sample, a cathodic photocurrent was not observed at 0 V. However, a starting anodic photocurrent takes place, probably originated from a hole charge carrier accumulation layer at this potential. As light-induced hole charge carriers cannot be efficiently extracted by the rear contact exhibiting Schottky-like behavior, these are accumulated in the vicinity of the space charge region and diffuse towards the surface giving rise to an oxidation reaction which results in the anodic photocurrent. For the annealed sample, a cathodic J_{ph} of -0.05 mA/cm² was obtained at -0.30 V. This value remains negligible compared to that observed at -1.75 V, which is around -17 mA/cm².

Catalytic activity of the photocatalyst was measured by Tafel slope at low potentials, from 0 to -0.5 V. For the annealed sample, the abrupt increase of J_{ph} over this potential range reflects a considerable low Tafel slope of 16 mV/dec compared to the ideal one of 60 mV/dec expected for semiconductor photoelectrodes, according with the Shockley-Read recombination model [34]. Even when low Tafel slopes are widely acknowledged as an indicator of efficient electrocatalytic performance, the extremely low J_{ph} in the range of 400 μ A/cm² indicates a slow surface reaction kinetics at these potentials.

The electrode kinetics at higher current densities near the saturation point (-17 mA/cm² at -1.75 V) reveals a higher Tafel slope of 120 mV/dec (Fig. 6). This distinction is of relevant importance considering systems such as water electrolyzers where high current densities at minimum operational potentials are required for economic viability [35]. A parallel recombination in the semiconductor bulk via charge carrier traps and within the space charge region has been found to lead into a Tafel slope between 60 and 120 mV/dec [36,37]. Therefore, the slope of 67 mV/dec observed in the as grown state, may be due to recombination processes in both regions, even at higher potentials. Thereby, inefficiently extracted photo-generated holes are accumulated between the bulk and the space charge region until their recombination takes place. On the other hand, for the annealed sample, it is interesting to note that the increase of the photocurrent density mainly occurs at low reverse bias potentials, from 0 to -0.5 V, and it starts to saturate at higher potentials, i.e. from -0.5 to -1.7 V.

An increment in dark current for the annealed sample is observed in Fig. 6 at high reverse bias potentials. To better perceive this phenomenon, Fig. 7 shows a magnification of the J-V curve, in

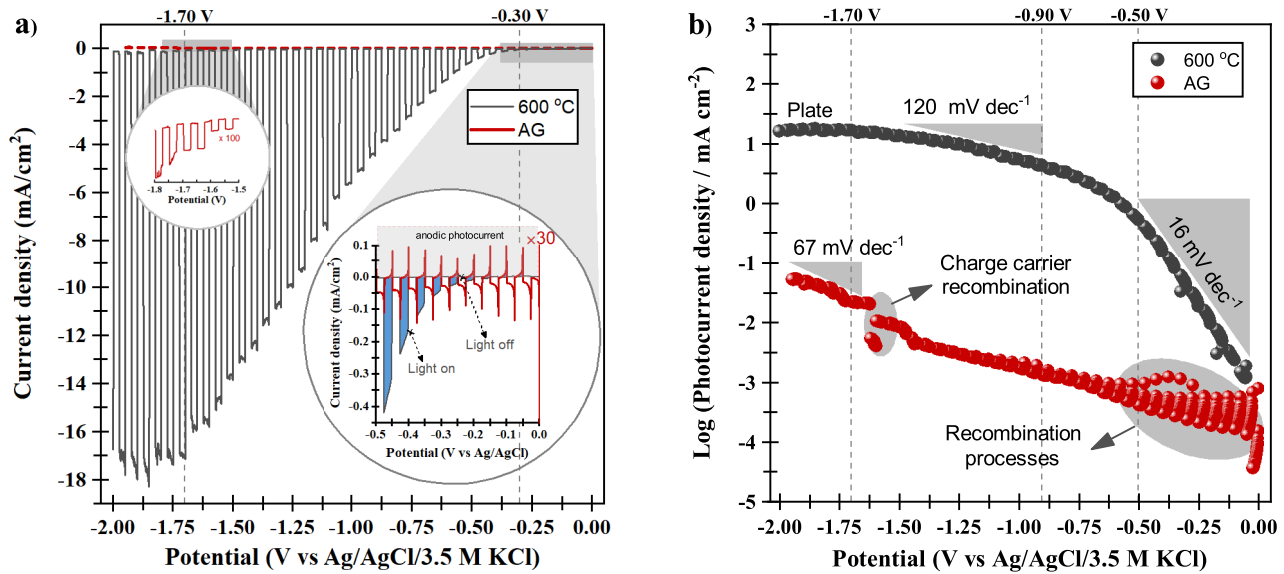


Figure 6. J-V polarization curves of c-Si(p)/a-SiC:H(p) for the as grown (AG) and annealed sample. Inset depicts a magnification of current at low reverse bias. -0.3 V is the potential from which appreciable photocurrent is observed, whilst -1.7 V is the potential at which photocurrent saturation is observed (a). Steady-state polarization curves were obtained by taken logarithm of the photocurrents. The Tafel regions identified are indicated by the triangular features. Recombination processes are appreciated for the sample AG as an unstable current, at low and high bias. For the annealed sample: -0.5 V is the potential at which photocurrent starts to saturate, -0.9 V sets the potential at which a change in Tafel slope is detected. At -1.7 V , photocurrent reaches saturation (b).

dark and under illumination, for this sample. The variation in dark current density is linked to a change in the semiconductor surface. In particular, the increment in the dark current might be associated to the native SiO_2 surface layer reduction. Evidence of the SiO_2 reduction at the thermodynamic standard potential of -0.857 V vs. NHE (-1 V vs. Ag/AgCl 3.5 M KCl) [38] may explain recombination processes observed in dark conditions, specifically from -1 V to higher potential values. The origin of this recombination might be attributed to a competition between hydrogen reduction, under high reverse bias potentials in the dark, and the SiO_2 surface layer reduction. Furthermore, several studies have reported UV-induced degradation of SiO_2 [39–41], decreasing the overpotential at the interface. Overall, a considerable evolution in the current density recorded under illumination is observed at the same potential at which the dark current density increases as a result of the SiO_2 reduction. This last feature is observed in the inset of Fig. 7.

The design of passivation strategies to suppress photogenerated charge carriers recombination includes the use of SiO_2 or wide bandgap semiconductors or insulators, such as Al_2O_3 . Thus, the passivation methods are typically addressed by depositing a few atomic layers of the oxide on photoelectrode surfaces. Moreover, in order to allow pinning of the band edges in an ideal situation, depicted in Fig. 8, passivation

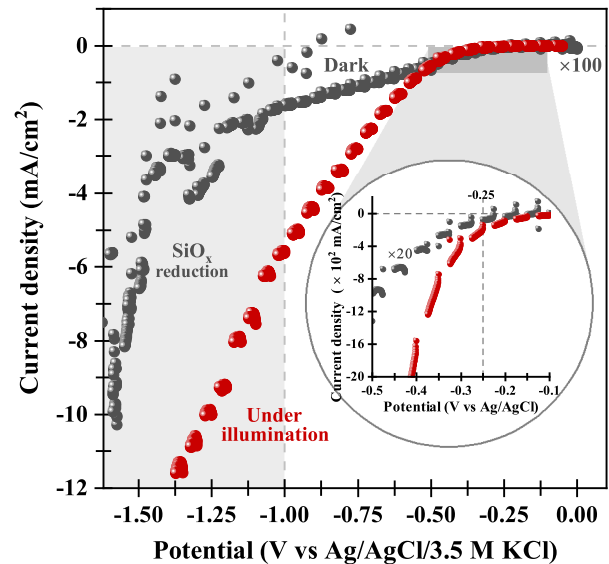


Figure 7. J-V current density for the $600\text{ }^\circ\text{C}$ annealed c-Si(p)/a-SiC:H(p) photocathode in the dark (gray curve) and under illumination (red curve). There is a noticeable abrupt increase of the J_{ph} at the potential in which the dark current density starts to raise, at -0.25 V .

layers may be ultrathin (1-2 nm) and dense [42]. Indeed, the compromise between the role of SiO_2 as a passivation layer and its performance as kinetic barrier at the semiconductor-electrolyte interface would be

interesting to investigate further. In order to gain a better understanding about the intrinsic SiO_2 influence on the photocurrent response of the p-type system, electrochemical impedance measurements will be discussed in the following section.

In Fig. 6, from -1.7V onwards, photocurrent saturation at $-17\text{mA}/\text{cm}^2$ is observed until -2V . This photocurrent limiting value might be associated to mass transport limitations occurred at high cathodic potentials. Thus, a high kinetics for electron transfer is assumed to take part at the semiconductor-electrolyte interface. Therefore, we propose a charge transfer process taking place via tunneling effect. This implies the fluctuating energy level maximum point of the electrolyte species (H^+/H_2) to be at a certain time, equal to the energy of the electron in the semiconductor [14]. This process is depicted in Fig. 8. For the system investigated, the ideal band edge pinned situation [43], would be reached upon application of potential values higher than -2.28V . This applied potential value ($V_{\text{ref}} - V_{\text{fb}}$) corresponds to the semiconductor potential of -1.7V .

The high J_{ph} achieved for the $600\text{ }^\circ\text{C}$ annealed sample at the potential range from -1.7 to -2V , suggests a mechanism photogenerated carriers from the p-type Si substrate, as depicted in Fig. 8. Thus, the achieved high electron transfer rate would be proportional to a high concentration of the relevant carrier in the semiconductor. In this case, for a p-type semiconductor device, i.e. c-Si(p)/a-SiC:H(p), and under illumination conditions, photogenerated electrons constitute the relevant carriers. The effect of the semiconductor relevant carriers in the current system is established by Eq. 4 [14]. In this equation, j_c^- is the cathodic current generated via the bottom of the conduction band, e is the elementary charge, κ_c^- is a quantum-mechanical tunneling coefficient, which depends on kinetic factors, n_s is the surface concentration of electrons in the conduction band, $[\text{H}^+]$ is the proton concentration in the electrolyte solution and W_{H^+} represents the distribution probability of the proton ion energy.

$$j_c^- = e\kappa_c^- n_s [\text{H}^+] W_{\text{H}^+} (E_c^s). \quad (4)$$

Concerning the mechanism depicted in Fig. 8, a previous study reported by Q.-B. Ma et al [16], indicates that due to the small barrier of conduction bands between p-Si and p-SiC, a few photogenerated electrons from the Si substrate can jump into the SiC with high external negative bias by means of tunneling effect. These electrons (n_s) can move towards the SiC surface to conduct hydrogen evolution reaction before recombination, and thus contribute to the photocurrent increment, according to Eq.4. This mechanism is also supported by electrochemical

impedance spectroscopy measurements as will be shown hereafter.

3.3.1. Electrochemical Impedance Spectroscopy In order to correlate the photocurrent features with the semiconductor-electrolyte interface structure under testing conditions, information of the system capacitive behavior for the annealed sample was retrieved from EIS. For an ideal system, simplified to a resistor (R) and a capacitor (C) in series, a plot of $1/C_{\text{SC}}^2$ vs electrode potential yields a straight line, known as Mott-Schottky plot. The line is extrapolated to $1/C_{\text{SC}}^2 = 0$ to determine the flat band potential V_{fb} . Here, V_{fb} is approximately 0.58V for the c-Si(p)/a-SiC:H(p) at $600\text{ }^\circ\text{C}$ annealed sample. The acceptor density (N_A) was estimated from Mott-Schottky plot (Fig. 9) using Eq. 5.

$$\frac{1}{C_{\text{SC}}^2} = \frac{2}{e\epsilon_0\epsilon_r A^2 N_A} \left(V - V_{\text{fb}} - \frac{\kappa T}{e} \right) \quad (5)$$

Here C_{SC} represents the space charge region (SCR) capacitance, ϵ_0 is the permittivity in vacuum, ϵ_r is the relative permittivity of a-SiC:H(p), A is the exposed area of the photocathode, κ is the Boltzmann's constant and T the temperature of the electrolyte.

According to Eq. 5, the V_{fb} is ideally not dependent on the frequency applied in Mott-Schottky measurements. However, and particularly for amorphous semiconductors, the presence of surface states is known to cause frequency dispersion in Mott-Schottky plots [44]. This is due to the contributions from surface states capacitance (C_{SS}) and double-layer capacitance (C_{dl}) to the apparent value of the space charge region capacitance (C_{SC}). That is actually the behavior observed for the annealed c-Si(p)/a-SiC:H(p) sample in Fig. 9. Two behaviors from this frequency dependent data can be distinguished. For high frequencies, i.e. 50 and 60 kHz , the fit lines seem to converge in a common intercept, and hence, yield what we believe a valid V_{fb} at around 0.585V . Whilst, for low frequencies, at 30 and 40 kHz , since slope values are quite similar compared with those observed at 50 and 60 kHz , a more reliable carrier concentration at around $2.7 \times 10^{15}\text{ atoms}/\text{cm}^3$ was extracted from these lower frequency data.

Slightly doped semiconductors are considered to vary in the range of 10^{16} to $10^{17}\text{ atoms}/\text{cm}^3$ compared with those heavily doped which exhibit values at around 10^{18} and $10^{19}\text{ atoms}/\text{cm}^3$ [43]. In the former case, the charge needed for Fermi level equilibration must come from deep inside the solid in contrast to the heavily doped case. Thus, the magnitude of the space charge layer width (W) will be larger. In general, typical W values range between $5\text{-}500\text{ nm}$ according to

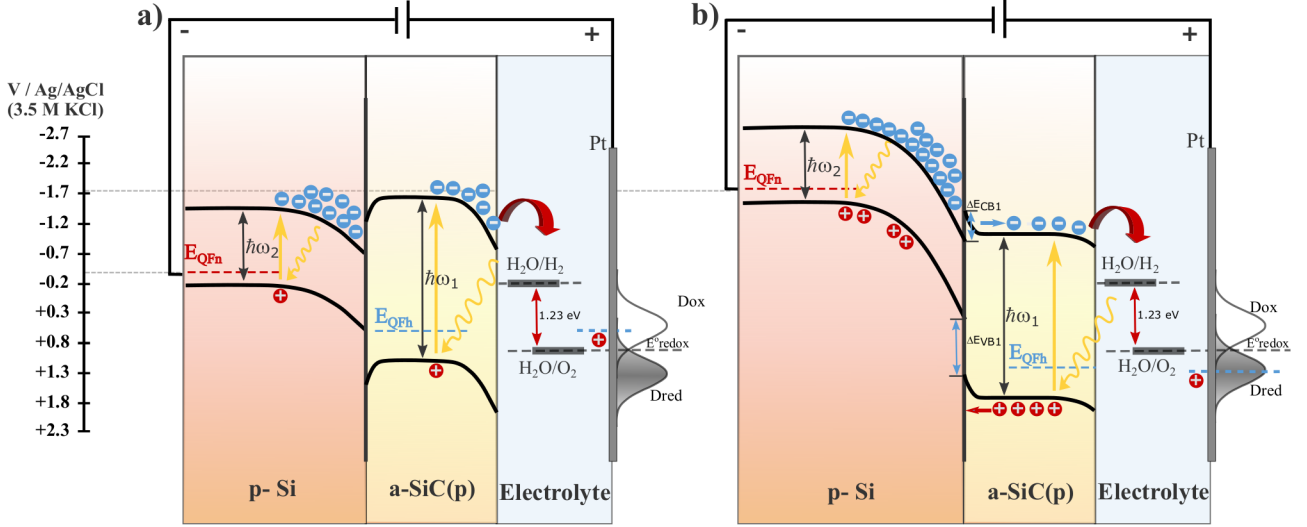


Figure 8. Energy band diagrams of PEC components: c-Si(p)/a-SiC:H(p) photocathode, anode (Pt) and light illumination, at an applied potential of -0.88 V (-0.3 V vs. Ag/AgCl 3.5 M KCl) (a) and under bias at -2.85 V (-1.7 V vs. Ag/AgCl 3.5 M KCl) in the ideal band edge pinned situation (b). E_{QFn} and E_{QFh} are the quasi-Fermi energy levels of electrons and holes, respectively. E_{redox}^o corresponds to the standard redox potential for oxygen evolution reaction taking place in the Pt counter electrode, whose fluctuation distribution of energy levels are D_{red} and D_{ox} .

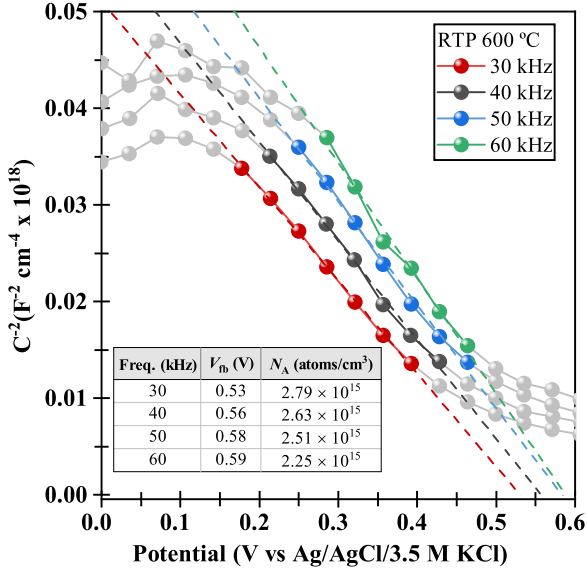


Figure 9. Mott-Schottky plots for the c-Si(p)/a-SiC:H(p) heterojunction annealed at 600 °C at frequencies of 30, 40, 50 and 60 kHz. The inset table shows the flat band potential and carrier concentration values obtained from the linear fits performed for each frequency data.

Eq. 6.

$$W = \sqrt{\frac{2\epsilon_0\epsilon_r}{eN_A} \left(\phi_{SC} - \frac{\kappa T}{e} \right)} \quad (6)$$

Here, based on minimum and maximum N_A values calculated from Mott-Schottky plots, the space charge width was estimated to be in the range from

390 to 435 nm. This estimation was made taking 2.79×10^{15} and 2.25×10^{15} atoms/cm³ as N_A , with a $\epsilon_r = 13.12$ [45], $T = 304.7$ K and a space charge potential drop $\phi_{SC} = 0.27$ V. Thus, for a low carrier concentration in the bulk of the semiconductor, the depletion of the entire 265 nm a-SiC:H(p) annealed layer takes place at all applied potential values. This effect supports the charge transfer mechanism assisted by photogenerated carriers from the Si substrate, as depicted in Fig. 8.

Fig. 10 depicts a potential-independent space charge region capacitance (C_{SC}) for the annealed a-SiC:H(p), which is a typical feature of insulators. The equivalent circuit model applied to extract these values is shown in Fig. 11. Nevertheless, the J-V curve obtained under illumination does not reflect such insulating behavior (Fig. 6). This evidence supports the theory of indirect charge transfer via SS reported initially by Salvador and Gutierrez and further studied for α -Fe₂O₃ photoanodes by Betoluzzi and Bisquert [21]. In regards to this theory, the density of surface states and its relative position respect to the band edges, determine whether these states are involved in equilibrium contact formation or charge transfer interface reactions [34].

To further understand the influence of SS in the photocurrent response, AC impedance spectroscopy characterization without illumination was performed to detect the frequency response of the c-Si(p)/a-SiC:H(p) heterojunction and identify its equivalent circuit. Nyquist plot fits (see supporting information), were performed with a parallel connection

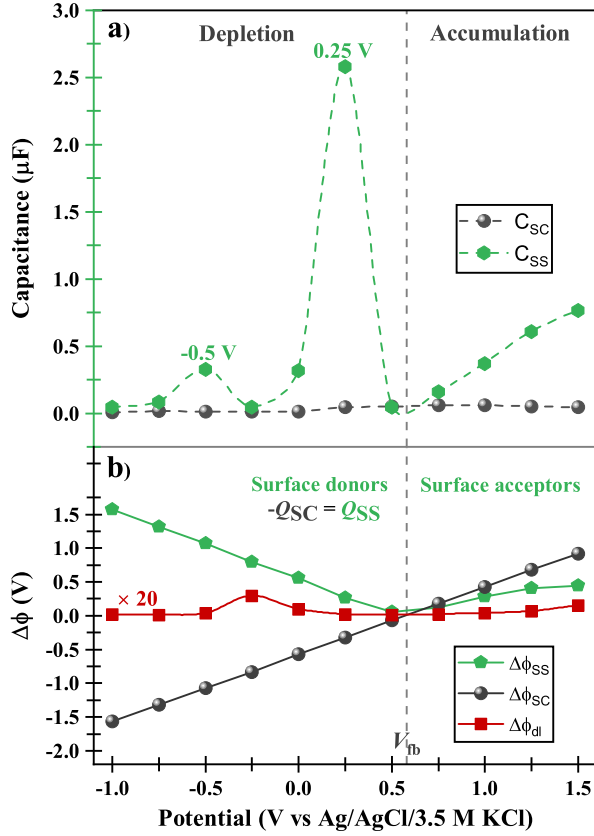


Figure 10. Simulated capacitance variation of the space charge and surface states upon applied potential for the annealed sample (a). Potential drop across the space charge, the double layer and surface states is shown (b). Negligible potential changing is observed across the double layer ($C_{dl} \gg C_{SC}$), whose potential values are scaled 20 times up for viewing purposes.

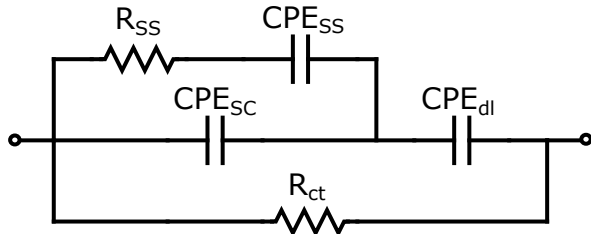


Figure 11. Equivalent circuit of the semiconductor-electrolyte interface used to simulate any charge transfer process in the dark. R_{SS} indicates the relaxation time for surface states, CPE_{SS} is the non-ideal surface state capacitance represented by a constant phase. CPE_{SC} and CPE_{dl} are the space charge and double layer constant phase, respectively. R_{ct} is the charge transfer resistance.

in addition to the series connection settled between the SCR and double layer capacitances [46]. This parallel capacitance represents surface states capacitance which in principle appears in parallel with that of the SCR.

In this study, a constant phase element (CPE)

was introduced as representation of the capacitance in the plot analysis. After performing circuit simulation by means of Multisim simulator program, values of potential drop (ϕ) were calculated for the SCR, double layer and surface states, treated at first approximation as a dielectric capacitance. When the AC bias is applied with respect to the reference electrode, the potential difference is expected to be distributed over the space charge and double layers. However, because $C_{dl} \gg C_{SC}$, any change in applied bias falls linearly across the semiconductor SCR (see Fig. 10). For the c-Si(p)/a-SiC:H(p) system, upon application of negative potentials respect to the V_{fb} (0.58 V), majority carrier density is depleted with respect to the bulk concentration. As a result, ϕ_{SC} increases towards more negative potentials in this region. In contrast, upon subjecting the electrode to anodic potentials, hole charge carrier density at the surface becomes much larger than those in the bulk and an accumulation layer appears.

The apparent potential drop depicted in Fig. 10 can be easily attributed to the variation of carrier concentration in SS, since these act as chemical instead of dielectric capacitances. In dielectric capacitances, the charge stored is associated to an electric field produced by spatial charge separation. This is the case for space charge and double layer capacitances [47]. On the other hand, in chemical capacitances, the charge storage associated mechanism is due to the variation of carrier concentration or chemical potential, as it is the case of surface states capacitances.

For this analysis, a frequency of 0.2 Hz was chosen to simulate a time scale slow enough and hence to be able to see any possible effect of surface state capacitance in charge transfer processes. The depletion zone depicted in Fig. 10, shows that $\Delta\phi_{SS}$ is compensated in magnitude by a further potential drop inside the semiconductor (gray solid line) rising in the opposite polarization. These results can be interpreted according to the charge neutrality condition, namely that the charge of the surface states Q_{SS} is compensated by an opposite charge inside the semiconductor layer. This condition is depicted in Figs. 12 and 13 for depletion and accumulation conditions of the SCR, respectively.

As shown in Fig. 12, under depletion condition, overall neutrality requires the presence of surface donors and therefore $Q_{SS} = -Q_{SC}$ [48]. On the other hand, the accumulation condition on p-type semiconductor, shown in Fig. 13, requires the presence of acceptor-like surface states, $-Q_{SS} = Q_{SC}$. Differences in the slope values of $\Delta\phi_{ss}$ curve, depicted in Fig. 10 are related to filling/unfilling of surface donors (in the depletion zone) and acceptors (in the accumulation zone). These differences would

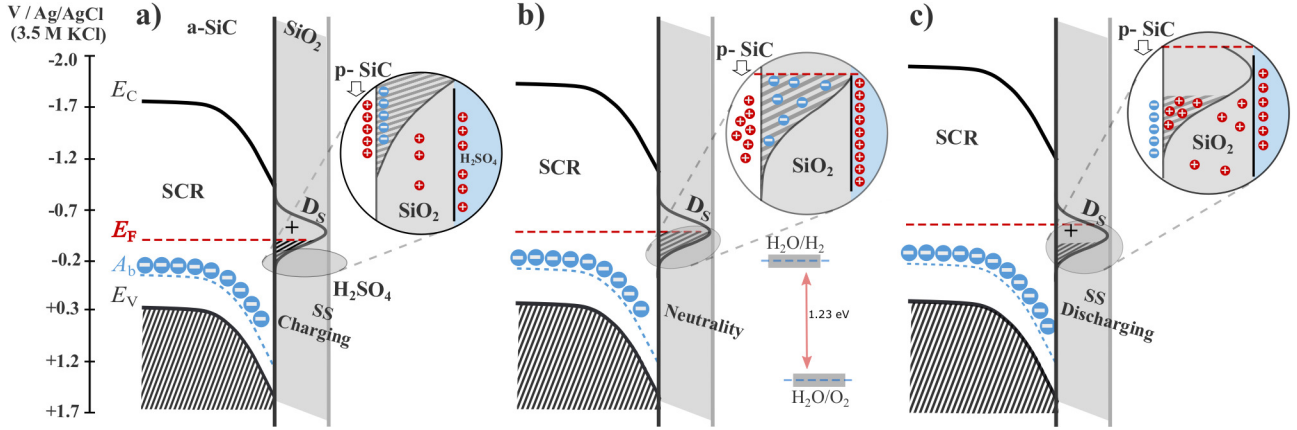


Figure 12. Energy band diagram and schematic of the c-Si(p)/a-SiC:H(p)/Surface states/ H_2SO_4 1 M electrolyte junction in a state of depletion under donor-like surface states (D_S) charging (a), neutrality condition (b) and surface states discharging (c). Where E_C is the conduction band energy, E_V the valence band energy, E_F the Fermi level and A_b the bulk acceptors energy level. Thermodynamic redox potentials for hydrogen and oxygen evolution reactions, HER and OER respectively, are shown following the same energy scale. Note that thermodynamic requirement for HER is achieved as hydrogen redox potential is fixed below D_S .

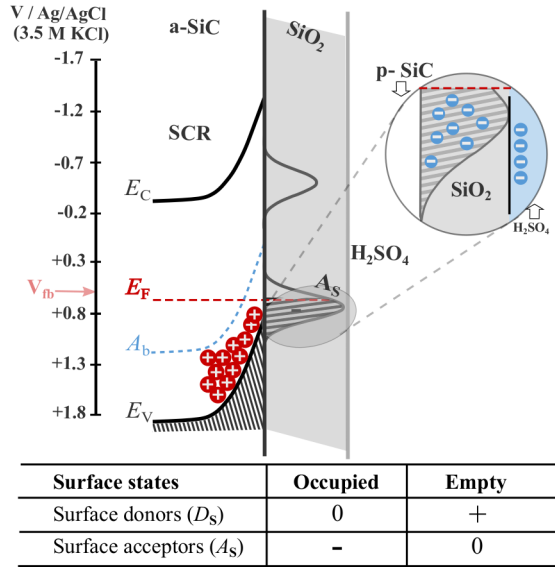


Figure 13. Energy band diagram and schematic of the c-Si(p)/a-SiC:H(p)/Surface states/ H_2SO_4 1 M electrolyte junction in a state of accumulation. The presence of an accumulation layer in p-type semiconductors requires partially filled acceptor-like surface states (A_S).

reflect the behavior of surface states preferably as charge donors (higher slope of potential drop vs applied potential) rather than acceptors (lower slope of potential drop vs applied potential). Fortunately, this donor-like behavior is desirable for water splitting purposes using p-type semiconductors.

Charging/discharging phenomena of surface states and their electronic influence in the vicinity of the SCR are also depicted in Figs. 12 and 13. In these, the electronic influence of the electrolyte in the interface has been considered. Thus, owing to the equilibrium

with the electrolyte, the neutrality condition of $Q_{SC} + Q_{SS} + Q_{dl} = 0$ is fulfilled. Magnifications illustrate the influence of donors (Fig. 12) and acceptors (Fig. 13) surface states in the SCR electronic behavior. Fig. 12 depicts this particular effect when the E_F crosses the SS energy band towards more negative potentials.

Fig. 14 shows the potential dependant surface state charge whose corresponding capacitance distributions are shown in Fig. 10. For comparison, the Mott-Schottky curve is plotted in the same figure. Since Mott-Schottky plots are obtained using AC impedance techniques, surface states will have an impact on the observed response. A correlation between the discharging of donor-like surface states with the electron enhancement inside the SCR is clearly observed in the distribution centered at -0.5 V. Therefore, a negative slope in the Mott-Schottky plot appears in the potential range from -0.5 V to \sim -0.9 V where surface states are being discharged. The opposite is true for the SCR populated with holes from -0.5 to 0 V, where movement of majority carriers towards the SCR upon charging of surface states takes place, in such a case a positive slope in the Mott-Schottky plot is observed. These slope variations in the depletion zone are well correlated to the SS charging/discharging mechanisms depicted in Fig. 12.

The highlighted fluctuation in the semiconductor capacitance across the depletion region depicted in Fig. 14 is attributed to the surface state capacitance whose charge distribution extends around 0.25 V. This evidences a Fermi level alignment between the top a-SiC:H p-type layer and surface states at its maximum point of energy distribution, which here has been found to be at \sim 0.25 V, as corroborated by Open Circuit Potential (OCP) measurements in the dark, at around

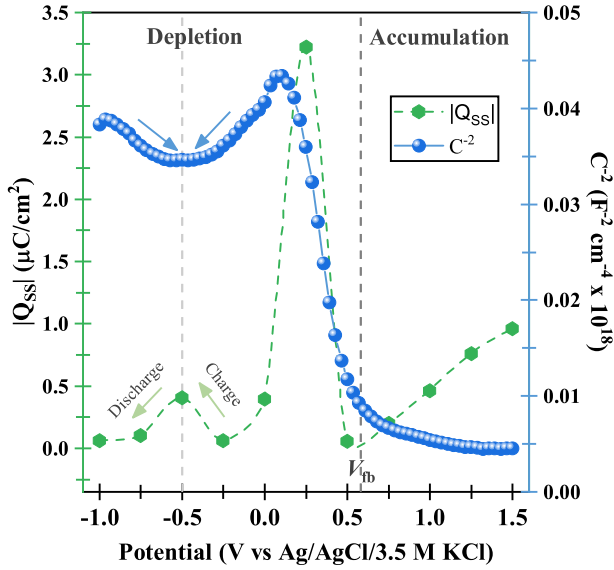


Figure 14. Mott-Schottky plot at frequency of 50 kHz and potential-dependent charge in surface states. Surface states charge distributions centered at -0.5 V and 0.25 V are correlated to the variation in the SCR electronic capacitance behavior observed in the Mott-Schottky plot.

0.3 V. According to previous studies [9], the maximum energy value for intrinsic a-SiC surface states would be positioned around 0.29 V.

In agreement with Mott-Schottky results and photocurrent potential-dependent response, it is likely that accumulation of electrons at surface states in the a-SiC:H(p) semiconductor is needed before a steady-state photocurrent for water reduction can be sustained. This first assumption is attributed to the location of surface states capacitance (starting at -0.25 V) that is slightly before the voltage at which appreciable photocurrent density appears (-0.3 V) (see Figs. 6 and 7).

As observed in Fig. 6, the increment of photocurrent occurs quickly from 0 to -0.5 V during surface states charging, meaning that at -0.5 V all these surface states are filled. Moreover, from -0.5 to -0.9 V, when surface states discharging takes place at the interface, an indirect electron charge transfer to the solution via surface states would be occurring to maintain the photocurrent at high density values. Once the Fermi level has crossed the whole energy band surface states, i.e. at around -0.9 V according to Q_{SS} curve, depicted in Fig. 14, charge transfer to the solution becomes slower. This is also reflected by a change in the Tafel slope, which rises up to 120 mV/dec. At this point, non-equilibrium or light induced formation and reoccupation of surface states may play a determining role in charge transfer processes and lead to a change in Q_{SS} and $\Delta\phi_{dl}$ as

well. This effect is what is called kinetic charging of the semiconductor surface or dynamic Fermi level pinning, which exhibits a characteristic Tafel slope of ~ 120 mV/dec, due to the fact that the applied potential falls across the electrochemical double layer, by means of the SS charging [14,34]. Here, this feature is observed in the potential range from -0.9 to -1.7 V.

4. Concluding remarks

In this work a systematic study of the physical properties and photoelectrochemical behavior of c-Si(p)/a-SiC:H(p) heterojunction was carried out. The surface smoothing taking place at 600 °C could have led into homogeneous currents as well as into a depletion of recombination centers at the surface. Since root-mean-square roughness R_q values for the annealed samples were lower than the as grown one, and the electrolyte did not induce further changes in the surface morphology, then the photocurrent is not significantly affected by the change in the effective surface area. The presence of disorder-induced localized states in the bulk of the Al doped a-SiC:H in the photocathode system, does not seem to play a determinant role in the photocurrent increment. In fact, recombination of photogenerated carriers, prone to take place inside these bulk states, is overridden by the drift current produced due to the whole depletion of the a-SiC:H(p) volume. On the other hand, localized surface states would take part in a desirable mechanism of indirect electron charge transfer to the electrolyte, and thus, conduct hydrogen evolution reaction. Concerning the SiO₂ native layer, our findings suggest that the SiO₂ layer reduction triggers a favorable semiconductor-electrolyte interface. This interface exhibits less overpotential barriers which promotes photocurrent generation. Here, the a-SiC:H(p) native oxide was not actively removed. Thus, we believe that the annealing-induced abrupt enhancement in the photoelectrochemical performance of the c-Si(p)/a-SiC:H(p) photocathode is probably associated to the obtained ohmic contacts as well as the passivation effect due to the native oxide layer [31–33]. Additional studies are necessary to assess the influence of annealing treatments on the a-SiC:H(p) semiconductor surface.

Acknowledgments

This research was funded by FONDECYT (National Fund for Scientific, Technological Development and Technological Innovation) under the agreement 147-2017. The author M. Mejia has been supported by the CONCYTEC Perú (National Council for Science, Technology and Technological Innovation) doctoral scholarship under the contract number

236-2015-FONDECYT as well as by the PUCP vicechancellorship for research (VRI, project no. CAP-2019-3-0041/702). The authors would like to thank the Katholischer Akademischer Ausländer-Dienst institution (KAAD) for the short-term grants given to conduct research internships in the Technische Universität Ilmenau (TU Ilmenau). Finally, the authors would like to thank the German Research Foundation (DFG) (DFG-Gz: INST 273/56-1 FUGG) and the Materials Characterization Center (CAM) at PUCP, for the financial support to conduct the characterization experiments.

5. Bibliography

- [1] A. Craig et al, Light, Water, Hydrogen The Solar Generation of Hydrogen by Water Photoelectrolysis, (Springer, Pennsylvania, 2008), p. 546.
- [2] W-H. Cheng et al, ACS Energy Lett. **3**, 1795-1800 (2018).
- [3] J. Gao et al, Joule **3**, 1-12 (2019).
- [4] P. Varadhan et al, Nat. Commun **10**, 1-9 (2019).
- [5] T.J. Jacobsson et al, Energy Environ. Sci. **6**, 3676–3683 (2013).
- [6] C. Jiang et al, Chem. Soc. Rev. **46**, 4645-4660 (2017).
- [7] B. Turan et al, Nat. Commun. **7**, 12681 (9pp) (2016).
- [8] A. Iwase et al, ChemSusChem **10**, 4420-4423 (2017).
- [9] I. Digdaya et al, Energy Environ. Sci. **8**, 1585-1593 (2015).
- [10] D.H. Van Dorp, H. Dennis and Hijnen, Angew. Chem. **48**, 6085-6088 (2009).
- [11] M.H. Kao et al, Sci. Rep. **7**, 1-8 (2017).
- [12] A. Madan et al, Annual Progress Report (DoE), 167-170 (2011).
- [13] M. Koper, J. Electroanal. Chem. **660**, 254-260 (2011).
- [14] R. Krol and G. Michael, Photoelectrochemical Hydrogen Production (Springer, Delft, 2014), p. 321.
- [15] L. Han et al, Mater. Chem. A. **3**, 4155-4162 (2015).
- [16] Q.B. Ma et al, J. Power Sources **253**, 41-47 (2014).
- [17] F. Zhu et al, Philos. Mag. **89**, 2726-2739 (2009).
- [18] J. Hu et al, 23rd European Photovoltaic Solar Energy Conference and Exhibition, Valencia, Spain, vol. 20 (2008), pp. 69-72.
- [19] P. Salvador et al, J. Phys. Chem. **88**, 3696–3698 (1984).
- [20] P. Salvador et al, J. Electrochem. Soc. **131**, 326–336 (1984).
- [21] L. Bertoluzzi et al, J. Phys. Chem. Lett. **3**, 2517-2522 (2012).
- [22] L. Bertoluzzi et al, J. Mater. Chem. A **4**, 2873-2879 (2016).
- [23] M. Mejia et al, 2020 J. Phys. D Appl. Phys. <https://doi.org/10.1088/1361-6463/abc77a>.
- [24] A. Tejada et al, Appl. Opt. **58**, 9585-9594 (2019).
- [25] J. A. Guerra et al, J. Phys. D: Appl. Phys. **52**, 105303 (11pp) (2019).
- [26] J.A. Guerra et al, J. Phys. D Appl. Phys. **49**, 195102 (6pp) (2016).
- [27] S. Suganuma et al, J. Am. Chem. Soc. **130**, 12787–12793 (2008).
- [28] J. Bullo et al, Phys. Stat. Sol. (b) **143**, 345 (1987).
- [29] F. Zhang et al, Phys. Rev. B **46**, 4590–4594 (1992).
- [30] S. Gallis et al, J. Appl. Phys. **102**, 024302 (2007).
- [31] T.L. Biggerstaff et al, Appl. Phys. Lett. **95**, 23-26 (2009).
- [32] X.G. Zhang, Electrochemistry of Silicon and Its Oxide (Kluwer Academic Publishers, New York, 2004), p. 510.
- [33] Q.B. Ma et al, J. Phys. D Appl. Phys. **45**, 325101 (6pp)(2012).
- [34] S. Jimenez, Photoelectrochemical Solar Fuel Production-From Basic Principles to Advanced Devices, Interfaces and Thin Films (Springer, Castelló, 2016), p. 574.
- [35] B. E. Conway et al, Int. J. Hydrogen. Energ. **12**, 607–621 (1987).
- [36] Y. Tashibana et al, J. Phys. Chem. **100**, 20056-20062 (1996).
- [37] R. Memming, Semiconductor Electrochemistry, (Wiley, Rellingen, 2016), p. 470.
- [38] P. Anatolyevich, Silicon **6**, 109–116 (2014).
- [39] R. Reitano et al, Philos. Mag. B. **81**, 629-636 (2001).
- [40] B. Pivac et al, Vacuum. **71**, 135-139 (2003).
- [41] X. Omeime, Optik **127**, 599-602 (2016).
- [42] A.M. Cowley et al, J. Appl. Phys. **36**, 3212-3220 (1965).
- [43] K. Rajeshwar, Encyclopedia of Electrochemistry, Vol. 6 (Semiconductor Electrodes and Photoelectrochemistry) (The University of Texas at Arlington, Texas, 2007).
- [44] E. Barsoukov and J. R. Macdonald, Impedance Spectroscopy: Theory, Experiment, and Applications (Wiley, New York, 2005), p. 595.
- [45] K. Yoshinaga et al, J. Phys. Conf. Ser. **441**, 012040 (2013).
- [46] M. Perny et al, J. Electr. Eng. **65**, 174-178 (2014).
- [47] J. Bisquert, Nanostructured energy devices: equilibrium concepts and kinetics (CRC Press, Boca Raton, 2014), p. 352.
- [48] H. Lüth, Solid Surfaces, Interfaces and Thin Films (Springer, Garching, 2010), p. 338.

Graphical Table of Contents

GTOC image:

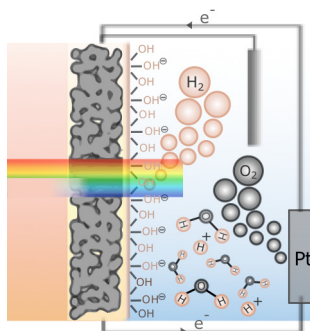


Figure 15. *

Localized states in amorphous absorber layers are commonly treated as recombination centers for solar-to-hydrogen energy conversion purposes. A model of indirect charge transfer to the solution via localized surface states taking place in c-Si(p)/a-SiC:H(p) photoelectrode device, has been evaluated under chopped light with an AM 1.5 solar standard, resulting in a high-quality performance as photocathode for water splitting